Journal of Photochemistry & Photobiology A: Chemistry 400 (2020) 112617

Contents lists available at ScienceDirect

Journal of Photochemistry & Photobiology A: Chemistry

journal homepage: www.elsevier.com/locate/jphotochem

A novel ternary Mica/TiO_2/Fe_2O_3 composite pearlescent pigment for the photocatalytic degradation of acetaldehyde

Xiangming Fang[a,b], Guanhong Lu[a], Asad Mahmood[a], Zhihong Tang[b], Ziwei Liu[a], Linlin Zhang[a], Yan Wang[a,*], Jing Sun[a,*]

[a] State Key Laboratory of High Performance Ceramics and Superfine Microstructure Shanghai Institute of Ceramics Chinese Academy of Sciences, 1295 Dingxi Road, Shanghai, China
[b] University of Shanghai for Science and Technology, 516 Jungong Road, Shanghai 200093, China

ARTICLE INFO

Keywords:
Photocatalytic composite pearlescent pigment
Mica-titania pigment
Gaseous acetaldehyde
Fe_2O_3

ABSTRACT

A novel ternary mica/TiO_2/Fe_2O_3 composite pearlescent pigment has been designed for the photocatalytic oxidation of gas-phase acetaldehyde in the application of indoor air purification. The mica/TiO_2/Fe_2O_3-x (MTF-x, x = m_{Fe2O3} : m_{TiO2} = 0.5–2: 100) composites were synthesized by a sol-gel assisted hydrothermal method. The MTF-1.5 composite shows optimal photocatalytic performance, which is 1.8 times photodegradation efficiency and 2.2 times CO_2 mineralization efficiency higher than those of pure TiO_2. The enhanced photocatalytic performance of MTF-x (x = 0.5–2) composites could be associated with enhanced reflectivity of mica, which eventually improved the light absorption properties. Also, the presence of TiO_2/Fe_2O_3 heterostructure facilitated charge separation in the MTF ternary composite. Besides, superoxide radical was proven as the decisive active species for the degradation of gaseous acetaldehyde. This work provides a systematic approach to develop a potential multi-functional pearlescent pigment to purify indoor air.

1. Introduction

Volatile organic compounds (VOCs) are regarded as the primary source of indoor air pollution [1–3]. The VOCs i.e., acetaldehyde, is released by the building materials, which can cause throat irritation, shortness of breath, eye irritation, and chest tightness [4–6]. Therefore, many air pollutants removal technologies have been developed [7–9]. The photocatalytic oxidation is regarded as a promising way for indoor air purification [10,11]. However, the degradation and CO_2 mineralization efficiency of semiconductor photocatalyst, such as TiO_2, have been limited by its poor light harvesting and fast recombination of the photoinduced hole-electron pairs [12]. The constructing of heterojunction with cocatalysts is an effective way to overcome these issues, such as TiO_2/ZnO and TiO_2/Fe_2O_3 [13,14].

Fe_2O_3 is a good cocatalyst due to its availability, chemical stability, and low bandgap energy (2.2 eV), which has been proved to enhance the visible light performance of TiO_2 [15–18]. Lin et al. [19] synthesized heterostructured TiO_2@α-Fe_2O_3 core–shell nanoparticles, which had good photocatalytic dyes degradation performance. The band matching of TiO_2 and Fe_2O_3 promotes the migration and separation of photogenerated electron and hole pairs, thereby improving the photocatalytic activity. Banisharif et al. [20] synthesized Fe_2O_3-doped TiO_2 photocatalyst by ultrasonic-assisted co-precipitation method and studied the photocatalytic performance for the photodegradation of trichloroethylene in the air. Zhao et al. [21] prepared a TiO_2/Fe_2O_3 nanocomposite film by a chemical bath deposition method. The TiO_2 modified by Fe_2O_3 show higher photopotential and photocurrent values than those of unmodified TiO_2. The optimal Fe^{3+} is beneficial to reduce the recombination of photogenerated electrons and holes, also the one-dimensional nanostructure can enhance the transfer and transport of charge carriers. Moniz et al. [22] synthesized novel Fe_2O_3–TiO_2 nanocomposite by photo-deposition method. Compared with P25, the composite shows better photocatalytic activity for the complete mineralization of the toxic 2,4-D herbicide. The heterojunction of Fe_2O_3–TiO_2 is confirmed to enhance the separation of photogenerated charge carriers. These results suggest that the construction of TiO_2/Fe_2O_3 heterojunction can obviously improve the photocatalytic activity. In addition, the reflection effect has proved to be a promising method to increase light harvesting [23]. Mica, a stoichiometric formula $KAl_2(AlSi_3O_{10})(OH)_2$, has high reflectivity, which is a good potential cocatalyst.

In view of the relationship between structure fabrication and photocatalytic activity of photocatalyst, we develop a mica/TiO_2/Fe_2O_3 photocatalytic composite pearlescent pigment (MTF) to photodegrade

* Corresponding authors.
E-mail addresses: wangyan@mail.sic.ac.cn (Y. Wang), jingsun@mail.sic.ac.cn (J. Sun).

https://doi.org/10.1016/j.jphotochem.2020.112617
Received 9 February 2020; Received in revised form 24 April 2020; Accepted 3 May 2020
Available online 21 May 2020
1010-6030/

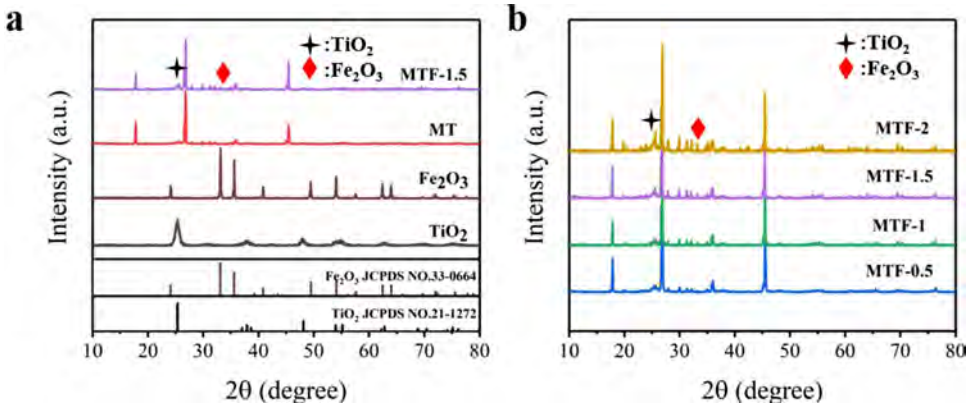

Fig. 1. (a, b) XRD patterns of pure TiO_2, Fe_2O_3, MT and MTF-x (x = 0.5–2) composites.

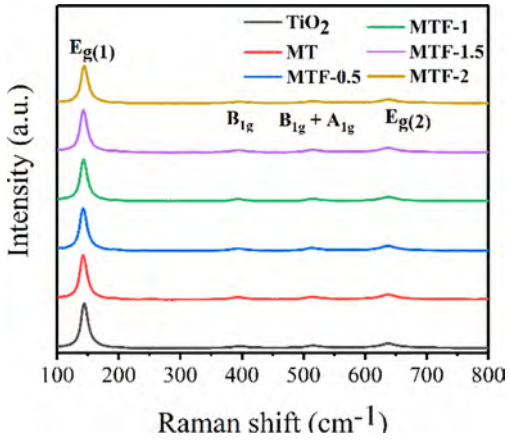

Fig. 2. Raman spectra of TiO_2, MT and MTF-x (x = 0.5–2) composites.

flowing gaseous acetaldehyde. The ternary composite is anticipated to improve the light harvesting, charge separation, and photodegradation efficiency. A sol-gel assisted hydrothermal method was used to synthesize MTF composite pearlescent pigments. In contrast to pure TiO_2, MTF demonstrate the obviously increased photodegradation of gaseous acetaldehyde efficiency and CO_2 mineralization activity. The optical characterizations i.e., UV-Vis, PL, and photocurrent studies suggest a synergistic effect in the ternary composite frameworks. The color property of MTF was characterized by the International Commission on Illumination (CIE) 1976 L*a*b* colorimetry. This work provides a facile approach to develop stable and efficient ternary photocatalytic composite pearlescent pigment, which can be exploited to develop a potential functional pigment for indoor air purification.

2. Experimental

2.1. Materials and reagents

The mica was purchased from Hangzhou Forward Fine Chemicals Co., Ltd, China. The acetaldehyde gas was purchased from Shanghai Weichuang Standard Gas Analytical Technology Co., Ltd. Tetrabutyl titanate and ferric chloride were purchased from Aladdin Industrial Corporation. All other chemicals and solvents were purchased from Shanghai Sinopharm Chemical Reagent Co., Ltd. (Shanghai, China) and used without further purification.

2.2. Synthesis

A sol-gel assisted hydrothermal method was used to prepare MTF photocatalytic composite pearlescent pigments. In a typical procedure, absolute ethanol (20 mL), tetrabutyl titanate (5 mL), and mica (3.9 g) were mixed by continuous stirring at room temperature (designated as solution A). Similarly, absolute ethanol (19 mL), concentrated nitric acid (0.1 mL), anhydrous ferric chloride (36 mg) and deionized water (1 mL) were mixed to form a solution (B). The solution B was slowly dropped into solution A, which were stirring to form a gel. The as-prepared gel was dried and homogenously dispersed in 70 mL deionized water by sonication. The suspension was then transferred into a Teflon-lined autoclave (100 mL) and maintained at 180 °C for 6 h. The final product was collected by centrifugation (6000 rpm) and washed three times with absolute ethanol and distilled water, which was named as MTF-1.5 (m_{Fe2O3}: m_{TiO2} = 1.5: 100 = 1.5 wt%). For comparison, the different mass amounts of $FeCl_3$, such as 12 mg, 24 mg, 36 mg, 48 mg, were added to solution B to prepare MTF-x (m_{Fe2O3}: m_{TiO2}: m_{mica} = 0.5–2: 100: 300) composites. Pure Fe_2O_3 was prepared as the same procedure without mica and tetrabutyl titanate. The mica-titania (MT) pearlescent pigment was prepared as the same procedure without $FeCl_3$.

2.3. Characterization

The phase development was studied using X-ray diffraction (XRD, BRUKER AXS GMBH, German) with a Cu Kα radiation source (λ = 0.154 nm). The surface, cross-sectional morphology and element mapping scan of composites were characterized by a Field Emission Scanning Electron Microscope (Magellan 400 FEI) at 10 kV operating voltage. The Brunauer–Emmett–Teller specific surface area (S_{BET}) were investigated by a Micromeritics ASAP 3000 nitrogen adsorption apparatus. All the composites were degassed at 300 °C for 12 h and then subjected to nitrogen adsorption measurements. Raman spectra were collected by DXR Raman Microscope (Thermo Fisher Scientific) using an excitation wavelength of 532 nm laser at 7 mW laser power. X-ray photoelectron spectroscopy (XPS) were carried out by a Microlab 310 F Scanning Auger Microprobe (VG SCIENTIFIC Ltd). The Perkin–Elmer Lambda 950 spectrometer was applied to record UV–Vis spectra of the samples ranging from 300 to 600 nm. The photoluminescence spectra (PL, Perkin–Elmer Luminescence spectrometer 55) of all the samples were acquired with an exciting wavelength of 320 nm. Electron spin resonance (ESR) signals of active radicals were recorded on a JES-FA200 spectrometer and trapped by 5,5-dimethyl-1-pyrroline N-oxide (DOJINDO Lab: > 99%) (DMPO). The photocurrent studies were carried out by a CHI660D electrochemical workstation using a conventional three-electrode cell configuration, which includes as a Pt counter electrode, Ag/AgCl as a reference electrode, and FTO coated with samples as a working electrode. The colorimetric values were evaluated in terms of the Commission Internationale de l'Eclairage (CIE) 1976 L*a*b* colorimetric method by a Color-Eye automatic differential colorimeter (XTS).

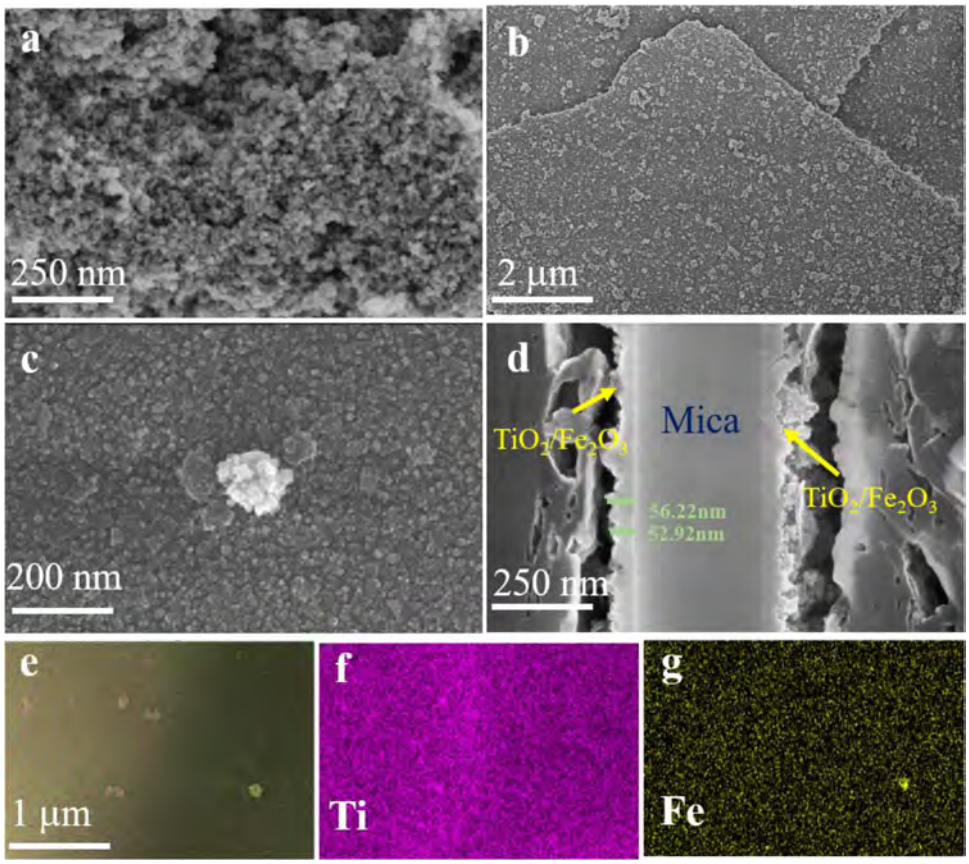

Fig. 3. SEM images of (a) pure TiO_2 and (b–c) MTF-1.5 composite, (d) cross-section SEM image of MTF-1.5 composite; EDS elemental mapping profiles of MTF-1.5 composite: (e) Ti-Fe overplay; (f) Ti atoms (purple); (g) Fe atoms (gold).

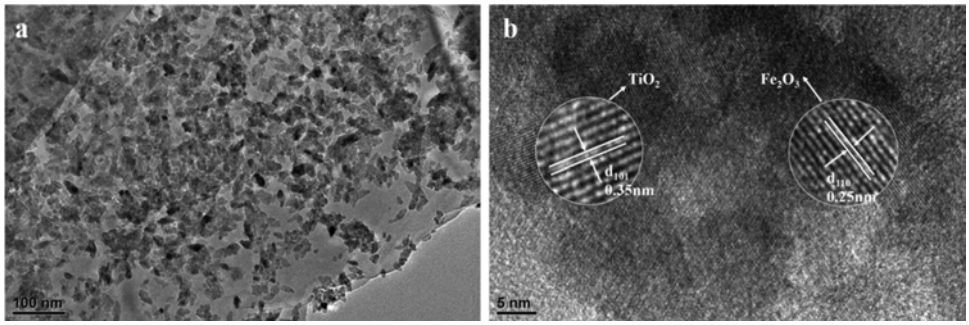

Fig. 4. (a, b) HRTEM images of MTF-1.5 composite.

2.4. Evaluation of photocatalytic activity

The photodegradation of acetaldehyde was carried out in an automated real-time gas-flow system coupled with a gas chromatograph (GC-7920). A 120 mL cuboid quartz vessel was used as the reaction chamber, which can be directly illuminated by the light source (400 W xenon lamp). The concentration change of gas acetaldehyde was recorded every 10 min. 0.1 g MTF-x (x = 0.5–2) composites for the photocatalytic reaction was dispersed in 2 mL ethanol, which were uniformly coated and dried on a glass plate (15 cm × 7.5 cm × 3 mm). The gas acetaldehyde was diluted one time by compressed air to stabilize the concentration at 500 ppm at 8 sccm flow rate. Initially, the adsorption-desorption equilibrium was achieved in the dark. Then, the samples were irradiated and the gas acetaldehyde concentration was monitored. The removal rate (η) of acetaldehyde was calculated by equation:

$$\eta = \left(1 - \frac{C}{C_0}\right) \times 100\%$$

Where C_0 is the initial concentration, and C is the acetaldehyde concentration at different times under irradiation. The yield of CO_2 was calculated by equation:

$$Y_{CO_2} = \frac{(CO_2)_{out} - (CO_2)_{in}}{2(C_2H_4O)_{in}}$$

Where $(CO_2)_{in}$ and $(CO_2)_{out}$, $(C_2H_4O)_{in}$ denoted the inlet and outlet concentrations of CO_2 and C_2H_4O, respectively.

3. Results and discussion

3.1. Phase structure and morphology

Fig. 1 shows the XRD analysis of pure TiO_2, Fe_2O_3, MT, and MTF-x

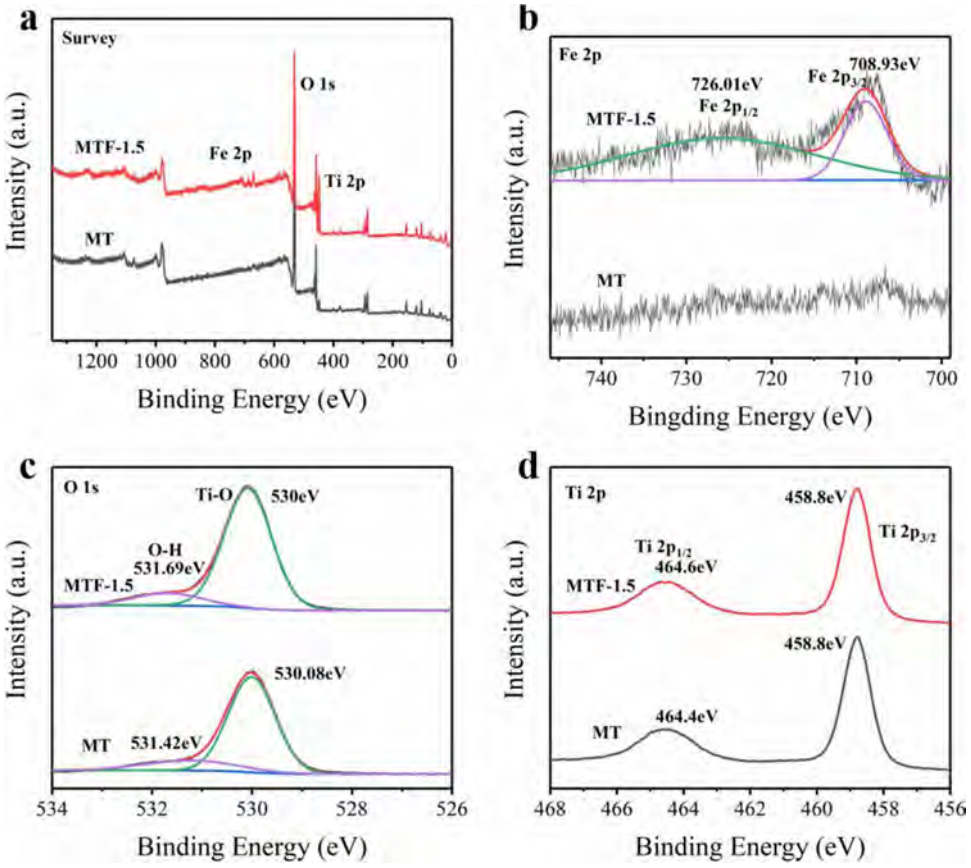

Fig. 5. XPS spectra of MT and MTF-1.5 composite: (a) survey spectrum, (b) Fe 2p, (c) O 1s and (d) Ti 2p.

Table 1
The color coordinates of MT and MTF-x (x = 0.5–2) composite pearlescent pigments.

Samples	Color coordinates			
	L*	a*	b*	ΔE*
MT	57.82	−0.71	−0.74	–
MTF-0.5	59.74	1.29	4.12	5.56
MTF-1	58.64	1.28	4.24	5.42
MTF-1.5	59.32	1.37	4.46	5.80
MTF-2	60.37	1.65	4.72	5.46

$\triangle E^* = \sqrt{(\triangle L^*)^2 + (\triangle a^*)^2 + (\triangle b^*)^2}$, where ΔL^*, Δa^* and Δb^* are the changes of L*, a*, and b* respectively.

(x = 0.5–2) composites. The characteristic peaks for potassium mica are observed at 2θ = 17.62°, 26.55°, 35.65°, and 45.03°, while the peak at 25.30° corresponds to anatase TiO_2. The diffraction peak at 2θ = 33.15° is attributed to (104) crystal plane of α-Fe_2O_3, whose intensity increases with the successive increasing of Fe_2O_3 contain in the MTF-x (x = 0.5–2) composites [24]. These results indicated that Fe_2O_3 was successfully introduced to MT.

The characteristic Raman modes of TiO_2 were observed at 144, 197, 399, 519, and 639 cm^{-1} as shown in Fig. 2, which correspond to $E_{g(1)}$, $B_{1g(1)}$, A_{1g} + $B_{1g(2)}$, and $E_{g(2)}$ of anatase TiO_2 and consistent with its XRD results.

The FESEM and EDS results of MTF-1.5 composite are illustrated in Fig. 3. The surface micrographs of pure TiO_2 indicated their average particle size below 30 nm in Fig. 3a. As shown in Fig. 3b and c, the MTF-1.5 composite demonstrated an irregular flat morphology with dozens of micron particle size and uniformly covered by nanoparticles. The cross-section morphology of MTF-1.5 composite is presented in Fig. 3d, whose inner layer is mica with about 300 nm thickness. And the outer layer of MTF-1.5 is uniform and its thickness is 54 ± 3 nm. To further confirm the presence of TiO_2/Fe_2O_3 heterojunction, the element mapping profile of MTF-1.5 composite has been tested. As shown in Fig. 3e–g, Ti and Fe atoms are uniformly distributed on the surface of mica. And the content of Fe atom is lower than that of Ti atom.

The HRTEM images were used to reveal the TiO_2/Fe_2O_3 heterojunction of MTF-1.5 composite (Fig. 4). As shown in Fig. 4b, the d-spacing is 0.35 nm corresponding to the (1 0 1) plane of cubic TiO_2 and the spacing is 0.25 nm belonging to the (1 1 0) plane of Fe_2O_3. Therefore, TiO_2/Fe_2O_3 with heterostructure uniformly coat on the surface of mica.

The XPS study was used to analyze the chemical composition and elemental chemical state of the MTF-1.5 composite (Fig. 5). The full range survey XPS spectrum of MT and MTF-1.5 composite are presented in Fig. 5a. The presence of Fe element in MTF-1.5 composite has been

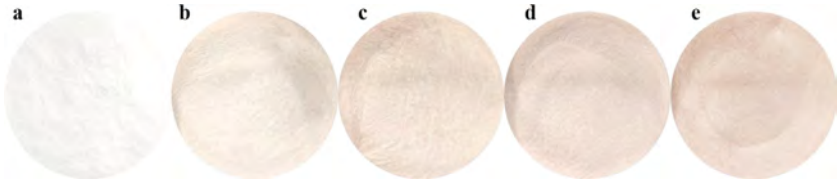

Fig. 6. The optical images of (a) MT, (b) MTF-0.5, (c) MTF-1, (d) MTF-1.5, (e) MTF-2 composites.

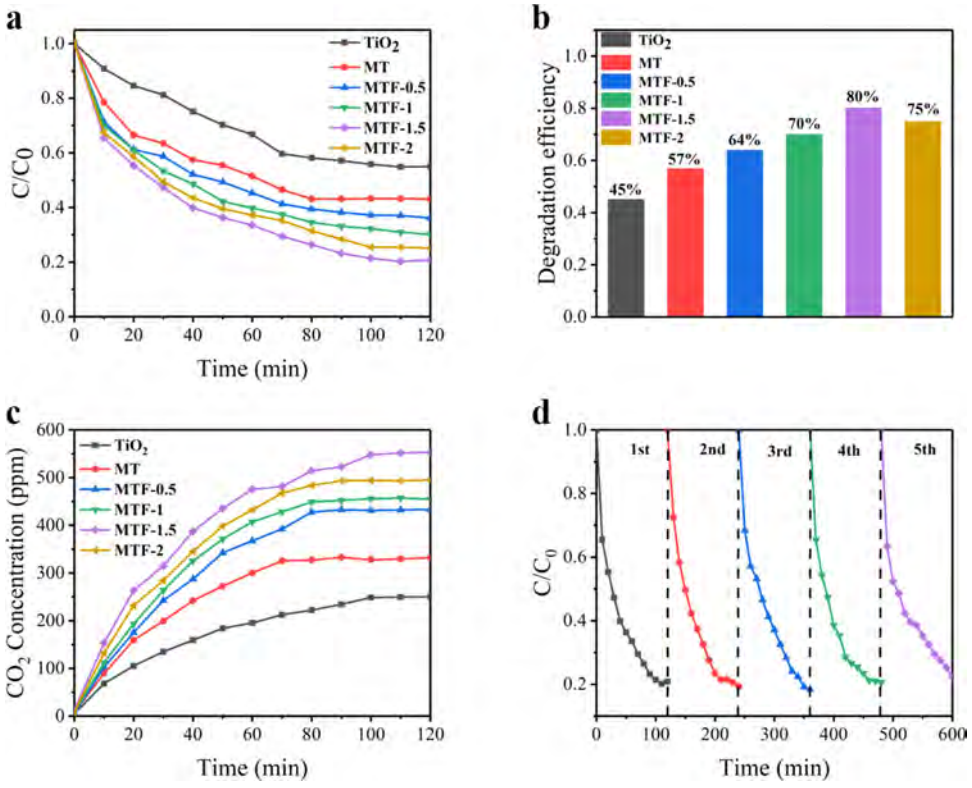

Fig. 7. (a, b) Photocatalytic degradation of flowing gaseous acetaldehyde (500 ppm, 8 sccm) under 400 W Xenon lamp irradiation; (c) Time profiles of CO_2 concentration of the composites; (d) Cyclic experiments with MTF-1.5 composite.

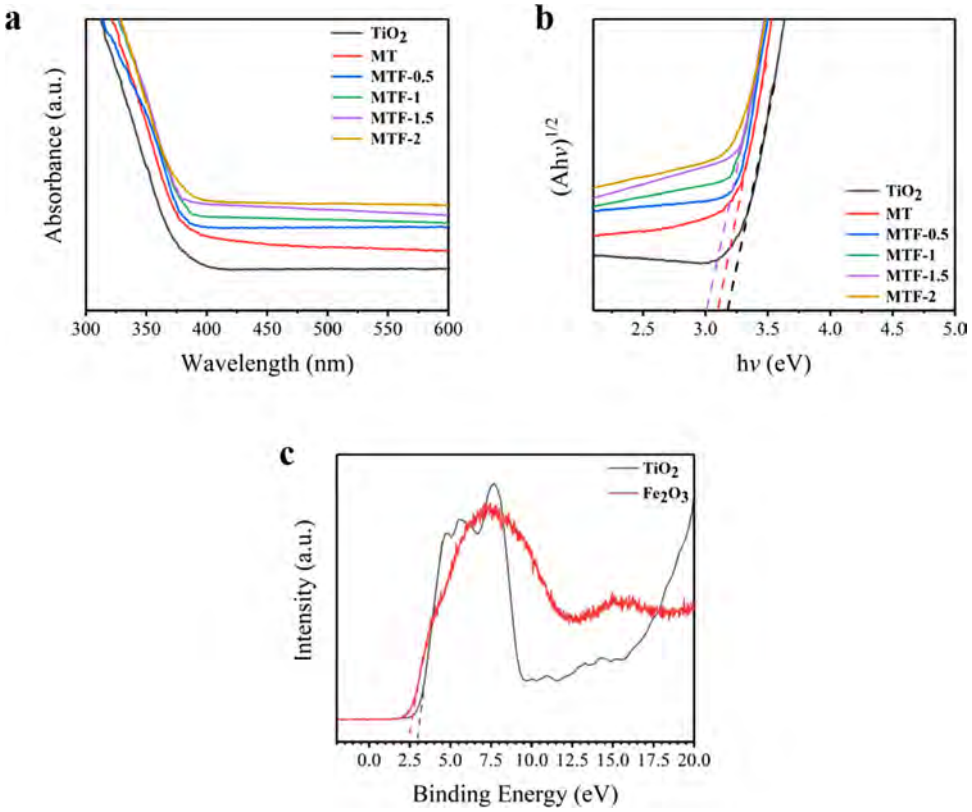

Fig. 8. (a) UV–Vis absorption spectra of pure TiO_2, MT and MTF-x (x = 0.5–2) composites; (b) The graph of the converted Kubelka–Munk function of light energy; (c) The XPS valence band spectra of TiO_2 and Fe_2O_3.

Table 2
The specific surface area of the as-prepared samples calculated by BET method.

Sample	TiO_2	MT	MTF-0.5	MTF-1	MTF-1.5	MTF-2
S_{BET} (m^2/g)	81.3	47.1	41.6	44.9	43.7	43.6

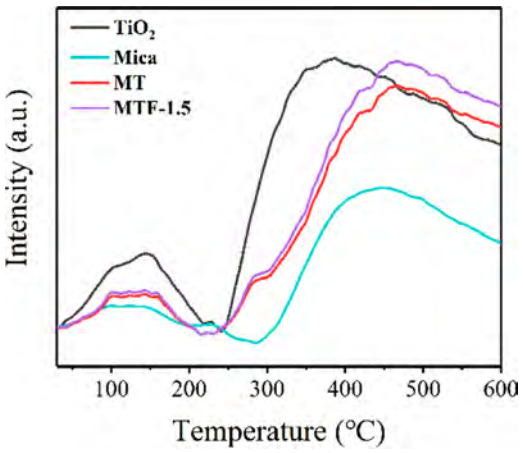

Fig. 9. TPD spectra of acetaldehyde of pure TiO_2, mica, MT and MTF-1.5 composite.

proved. In the case of Fe 2p (Fig. 5b), two peaks at 708.93 and 726.01 eV were fitted, which is attributed to Fe 2p3/2 and Fe 2p1/2, respectively. The energy difference between Fe 2p3/2 and Fe 2p1/2 is 17.09 eV, indicating the presence of a-Fe2O3 in MTF-1.5 composite [25]. For O 1s (Fig. 5c), the two peaks at 530 and 531.69 eV are attributed to Ti-O and O-H in MTF-1.5 composite. However, the binding energy of O–H bond in MTF-1.5 composite is higher than that of TiO2, which may provide an indirect evidence for the formation of the Ti–O–Fe bond [26]. As shown in Fig. 5d, the typical peaks of Ti 2p1/2 and Ti 2p3/2 in MT appeared at 464.4 eV and 458.8 eV. These binding energy peaks of MTF-1.5 composite were detected at 464.6 eV and 458.8 eV. The energy difference of Ti 2p1/2 and Ti 2p3/2 peaks in MT and MTF-1.5 composite were 5.6 eV and 5.8 eV, respectively. It is concluded that the energy difference of Ti 2p increase due to the formation of Ti–O–Fe bond in MTF-1.5 composite [27].

The MT pearlescent pigment is composed of TiO_2 deposited on mica sheets, which also shows good optical properties. CIE colorimetric analysis was used to characterize the optical properties of the composites. As can be seen from the data listed in Table 1, MTF-x (x = 0.5–2) composite pearlescent pigments show light red color effect ($1.29 < a^* < 1.65$, $4.12 < b^* < 4.42$). Compared with MT pigment, the L* (brightness) of the MTF-x (x = 0.5-–2) composite pearlescent pigments slightly increase, and ΔE* also increases with the increasing concentration of Fe_2O_3. It is worth noting that the higher L* value of MTF-x (x = 0.5–2) composite pearlescent pigments maybe imply superior light harvesting to enhance its photocatalytic performance (Fig. 6).

3.2. Photocatalytic activity measurement

The photocatalytic performance of pure TiO_2, MT and MTF-x (x = 0.5–2) composites are shown in Fig. 7. The photodegradation efficiency of pure TiO_2 is 45% (Fig. 7a) and 250 ppm of CO_2 were released at the same time (Fig. 7c). According to the equation ($Y_{CO_2} = \frac{(CO_2)_{out} - (CO_2)_{in}}{2(C_2H_4O)_{in}}$), the CO_2 mineralization efficiency of pure TiO_2 is 25%. The photodegradation efficiency of MT increase to 57% and CO_2 mineralization efficiency is 33% (red line). The MTF-1.5 composite (purple line) has the highest photodegradation efficiency (80%), which is 1.8 times higher than that of pure TiO_2 and 1.4 times higher than that of MT. And its CO_2 mineralization efficiency (55%) is 2.2 times higher than that of pure TiO_2 and 1.8 times higher than that of MT. Thus, it can be inferred that the photocatalytic performance of MT can be significantly enhanced by TiO_2/Fe_2O_3 heterojunction. A cyclic test of MTF-1.5 composite is further used to study the stability for practical device applications (Fig. 7d). The test was performed in two weeks in successive five cycles. The results show that the MTF-1.5 composite can maintain high photocatalytic stability after the fifth cycle, ensuring its long-term use.

3.3. Mechanism studies of photocatalytic degradation

3.3.1. Optical properties

The optical properties of pure TiO_2, MT and MTF-x (x = 0.5–2) composites were investigated by UV–Vis spectroscopy (Fig. 8). As shown in Fig. 8a, the absorbance of MT is higher than that of pure TiO_2 ranging from 300 to 600 nm due to the reflection of mica core. Besides, the absorbance of MTF-x (x = 0.5–2) composite increase with the increasing content of Fe_2O_3. Compared with MT, the absorption band edges of MTF-x (x = 0.5–2) composites demonstrate a red-shift, which extends light absorption in the visible region. This behavior can be associated with the narrow energy band of Fe_2O_3 and enhanced optical scattering in the ternary composite structures [28]. The bandgap energy of composite was calculated using equation of

$$(\alpha h\nu)^{1/n} = A(h\nu - E_g)$$

where α is the absorption coefficient, A is the parameter that is related to the effective mass associated with the valence and conduction bands, hν is the absorbed energy and E_g is the bandgap energy (Fig. 8b). The value of the index indicates the nature of the electronic transition, either directly or indirectly: the value of n is 0.5 for direct and 2 for

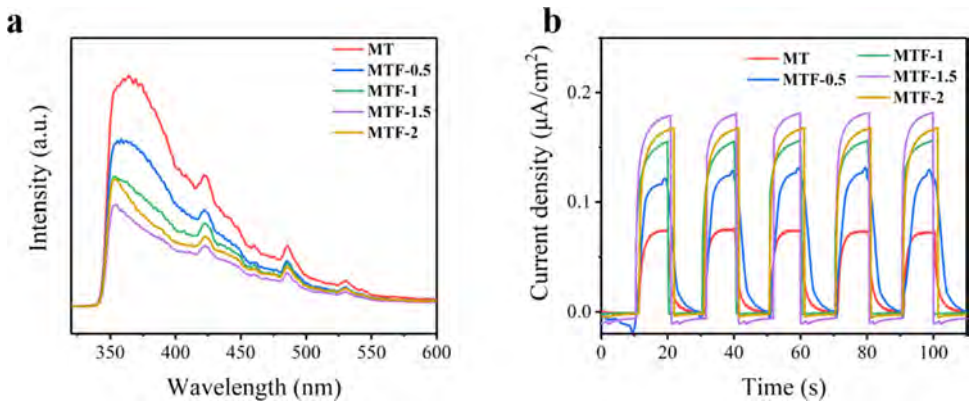

Fig. 10. (a) PL spectra and (b) Photo-current response of MT and MTF-x (x = 0.5–2) composites.

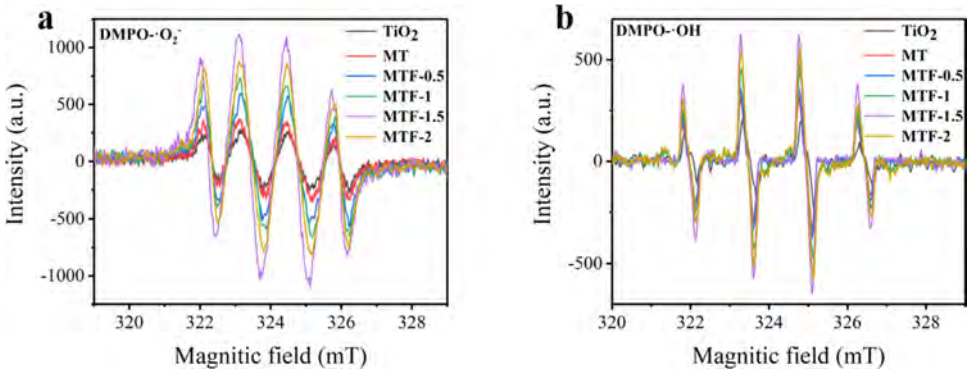

Fig. 11. (a) ·O_2– and (b)·OH detection of pure TiO_2, MT and MTF-x (x = 0.5–2) composites.

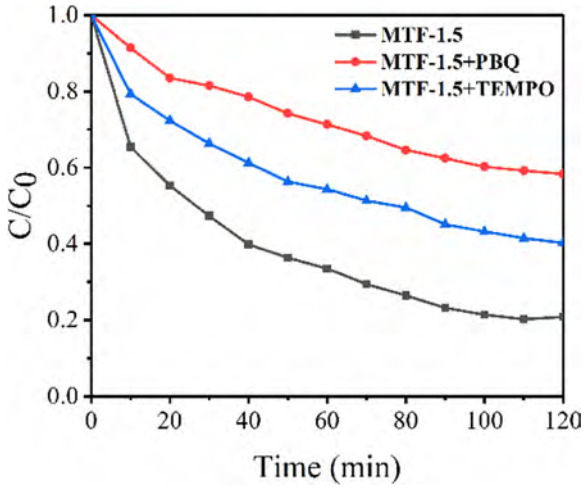

Fig. 12. Scavenger experiments using PBQ and TEMO as corresponding ·O_2^- and ·OH quenching.

indirect bandgap materials [29]. The E_g value of MT (3.1 eV) is lower than that of TiO_2 (3.2 eV), which is due to the inter-band electronic transitions from TiO_2 to mica [30]. The E_g value of MTF-1.5 composite is 3.0 eV. The XPS valence band spectra of TiO_2 and Fe_2O_3 have been presented in Fig. 8c. The valence band (VB) of a TiO_2 is 2.91 eV and the conductive band (CB) is −0.29 eV. While VB of Fe_2O_3 is 2.48 eV and CB is 0.24 eV, respectively.

3.3.2. The pollutant adsorption

The corresponding specific surface area (S_{BET}) of composites were employed to estimate the relationship between the adsorption ability of gas and photocatalytic performance. The bigger specific surface area (S_{BET}) value correspond to the larger number of adsorbed gas molecules of composites [31]. As shown in Table 2, the S_{BET} value of MTF-x (x = 0.5–2) composites ranging from 41.6 to 44.9 m^2/g are smaller than those of pure TiO_2 (81.3 m^2/g) and MT (47.1 m^2/g). It could be assumed that the introducing of micro flake mica and Fe_2O_3 is negative for increasing pollutant adsorption. The temperature programmed desorption (TPD) results of pure TiO_2, mica, MT and MTF-1.5 composite are shown in Fig. 9. The peak located at 100 − 200 °C is related to weak binding for physical absorption of acetaldehyde and the peak located at 300 − 500 °C is ascribed to strong chemical adsorption. The higher TPD intensity represented stronger adsorptive capacity. As presented in Fig. 9, the order of gas acetaldehyde physical adsorption is TiO_2 > MTF-1.5 ≈ MT > mica. While, the order of chemical adsorption is TiO_2 ≈ MTF-1.5 > MT > mica. And the quantity of chemically adsorbed acetaldehyde of the four samples are all stronger than that of physically adsorbed. In contrast to pure TiO_2, the desorption temperature of MT and MTF-1.5 composite both increase from 350 °C to 450 °C, which indicate the enhancing of chemical absorbability by introducing mica and Fe_2O_3. Hence, the chemical absorbability of photocatalyst could ultimately enhance the photocatalytic activity [32].

3.3.3. Photogenerated electron hole separation

The PL spectroscopy was used to investigate the separation efficiency of charge carriers in semiconductor [33,34]. The lower PL intensity represents less recombination. The emission intensity of MTF-x (x = 0.5–2) composites are much lower than that of pure TiO_2 (Fig. 10a), which indicates that the TiO_2/Fe_2O_3 heterojunction effectively inhibits the recombination of photogenerated charge carriers. The photocurrent test was used to characterize the generation and separation of photogenerated electron-hole pairs (Fig. 10b). Compared to MT, MTF-x (x = 0.5–2) composites exhibit higher photocurrent density, which means that more photoinduced e^- and h^+ pairs generation and separation were in MTF-x (x = 0.5–2) composites. It is positive for the increasing of photocatalytic performance [35].

3.3.4. The role of radicals

The electron spin resonance (ESR) test was employed to study the

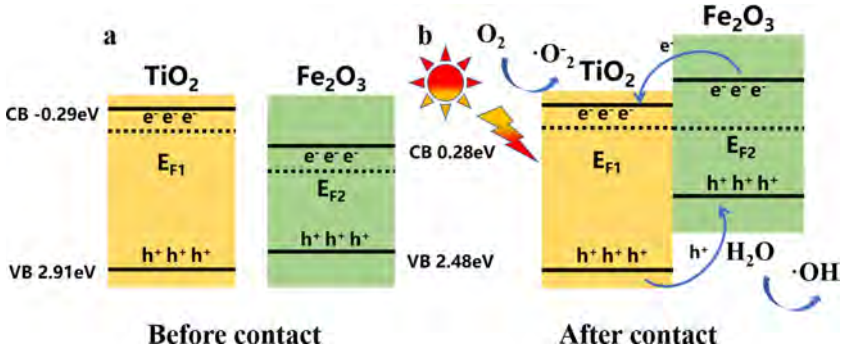

Fig. 13. Schematic diagram of the ternary structure of MTF composite.

role of superoxide radicals ($\cdot O_2^-$) and hydroxide (·OH) in Fig. 11 [36]. The stronger intensity of radicals presents more radical produced. The intensity order of $\cdot O_2^-$ and ·OH are both MTF-1.5 > MTF-2 > MTF-1 > MTF-0.5 > MT > pure TiO_2, which suggests that the TiO_2/Fe_2O_3 heterojunction and mica could promote the production of reactive radicals. Also, the intensity of $\cdot O_2^-$ of all samples are higher than that of ·OH. Therefore, it is anticipated that $\cdot O_2^-$ plays a leading role in the photodegradation of acetaldehyde of this work.

The scavenger experiment of MTF-1.5 composite was performed to further verify the role of $\cdot O_2^-$ and ·OH [37,38]. The $\cdot O_2^-$ scavenger is p-benzoquinone (PBQ) and ·OH scavenger is 2,2,6,6-tetramethyl-1-pi-peridinyloxy (TEMPO). The more photocatalytic performance decreased, the more important of corresponding radicals played. As shown in Fig. 12, the photodegradation efficiency of MTF-1.5 composite sharply decreased from 80% to 60% with PBQ or 42% with TEMPO, when photo-$\cdot O_2^-$ or ·OH are captured, respectively. Thus, it can be inferred that $\cdot O_2^-$ are more active in acetaldehyde degradation in contrast to ·OH, which is consistent with the results of ESR.

3.4. Mechanism of enhanced photocatalytic activity

Based on the results, we propose a possible mechanism for the enhanced photocatalytic performance of MTF ternary composite. As illustrated in Fig. 13, when TiO_2 contacts Fe_2O_3 to obtain an equalized Fermi level by heterojunction, the electrons flow from Fe_2O_3 to TiO_2. There is a positive region adjacent to TiO_2 in the heterojunction. While, the holes flow from TiO_2 to Fe_2O_3, resulting in the formation of a negative region adjacent to Fe_2O_3 in the heterojunction. Thus, an internal electric field is constructed between TiO_2 and Fe_2O_3 [39,40]. The electrons accumulated in the CB of TiO_2 will react with O_2 to form $\cdot O_2^-$, while the accumulated holes in the VB of Fe_2O_3 will react with H_2O and OH– to form ·OH. The adsorbed acetaldehyde was oxidized on the surface of the photocatalyst. In addition, mica serving as reflection core can further improve the light harvesting of TiO_2/Fe_2O_3 shell layer. Therefore, the synergy of mica, TiO_2 and Fe_2O_3 greatly enhances the ternary composite photocatalytic performance without decreasing its pearlescent effect.

4. Conclusion

In this work, a novel MTF-x photocatalytic composite pearlescent pigment was successfully synthesized by a sol-gel assisted hydrothermal method. The crystal structure, morphology, and optical properties of the product materials were studied. The UV–Vis results show that the light utilization efficiency can be improved by introducing the mica core into the ternary composite. Compared with TiO_2 and MT, MTF-x (x = 0.5–2) composite pearlescent pigments exhibited an enhanced photocatalytic performance. The MTF-1.5 composite demonstrated the highest photodegradation efficiency for acetaldehyde (80%) and CO_2 mineralization efficiency (55%) in this work. $\cdot O_2^-$ play a key role in the acetaldehyde photocatalytic degradation. Also, the photoinduced hole-electron pairs separation can be promoted by the TiO_2/Fe_2O_3 heterojunction. This work provides a facile route to develop a stable and efficient photocatalytic composite pearlescent pigment for acetaldehyde degradation, which exhibits a high degradation and conversion efficiency. The MTF composite pearlescent pigments can also be expected to degrade other VOCs for the indoor air purification as the functional decorative additive in the finish paint.

Author statement

We confirm that the manuscript has been read and approved by all named authors and that there are no other persons who satisfied the criteria for authorship but are not listed. We further confirm that the order of authors listed in the manuscript has been approved by all of us.

We confirm that we have given due consideration to the protection of intellectual property associated with this work and that there are no impediments to publication, including the timing of publication, with respect to intellectual property. In so doing we confirm that we have followed the regulations of our institutions concerning intellectual property.

We understand that the Corresponding Author is the sole contact for the Editorial process (including Editorial Manager and direct communications with the office). She is responsible for communicating with the other authors about progress, submissions of revisions and final approval of proofs. We confirm that we have provided a current, correct email address which is accessible by the Corresponding Author and which has been configured to accept email from wangyan@mail.sic.ac.cn.

Signed by all authors as follows: Xiangming Fang, Guanhong Lu, Asad Mahmood, Zhihong Tang, Ziwei Liu, Linlin Zhang, Yan Wang, Jing Sun Apr. 24th, 2020

Declaration of Competing Interest

The authors declare that they have no known competing financial interests or personal relationships that could have appeared to influence the work reported in this paper.

Acknowledgments

This work was financially supported by the National Key Research and Development Program of China (2016YFA0203000), National Natural Science Foundation of China (Grant No. 51702347) and Shanghai Municipal Committee of Science and Technology Research Project (Grant No. 19DZ1205102 and 18142201700).

References

[1] H.L. Chen, H.M. Lee, S.H. Chen, M.B. Chang, S.J. Yu, S.N. Li, Removal of volatile organic compounds by single-stage and two-stage plasma catalysis systems: a review of the performance enhancement mechanisms, current status, and suitable applications, Environ. Sci. Technol. 43 (2009) 2216–2227.
[2] S.S.H. Ho, Y. Huang, S.-C. Lee, J. Cao, Challenges on field monitoring of indoor air quality in china, Indoor Built Environ. 26 (2017) 576–584.
[3] Y. Liu, X. Zhu, Measurement of formaldehyde and VOCs emissions from wood-based panels with nanomaterial-added melamine-impregnated paper, Constr. Build. Mater. 66 (2014) 132–137.
[4] Q. Qian, C. Gong, Z. Zhang, G. Yuan, Removal of VOCs by activated carbon microspheres derived from polymer: a comparative study, Adsorption 21 (2015) 333–341.
[5] H. Destaillats, M. Sleiman, D.P. Sullivan, C. Jacquiod, J. Sablayrolles, L. Molins, Key parameters influencing the performance of photocatalytic oxidation (PCO) air purification under realistic indoor conditions, Appl Catal B-Environ 128 (2012) 159–170.
[6] C. He, J.J. Li, J. Cheng, L.D. Li, P. Li, Z.P. Hao, Z.P. Xu, Comparative studies on porous material-supported Pd catalysts for catalytic oxidation of benzene, toluene, and ethyl acetate, Ind. Eng. Chem. Res. 48 (2009) 6930–6936.
[7] X.Y. Zhang, B. Gao, A.E. Creamer, C.C. Cao, Y.C. Li, Adsorption of VOCs onto engineered carbon materials: a review, J. Hazard. Mater. 338 (2017) 102–123.
[8] S.H. Zhang, J.P. You, C. Kennes, Z.W. Cheng, J.X. Ye, D.Z. Chen, J.M. Chen, L.D. Wang, Current advances of VOCs degradation by bioelectrochemical systems: a review, Chem. Eng. J. 334 (2018) 2625–2637.
[9] Z. Wang, X.F. Xie, X. Wang, A. Mahmood, H.X. Qiu, J. Sun, Difference of photodegradation characteristics between single and mixed VOC pollutants under simulated sunlight irradiation, J. Photochem. Photobiol. A 384 (2019).
[10] H. Guo, H.-Y. Niu, C. Liang, C.-G. Niu, D.-W. Huang, L. Zhang, N. Tang, Y. Yang, C.-Y. Feng, G.-M. Zeng, Insight into the energy band alignment of magnetically separable $Ag_2O/ZnFe_2O4$ p-n heterostructure with rapid charge transfer assisted visible light photocatalysis, J. Catal. 370 (2019) 289–303.
[11] Y.-Y. Yang, X.-G. Zhang, C.-G. Niu, H.-P. Feng, P.-Z. Qin, H. Guo, C. Liang, L. Zhang, H.-Y. Liu, L. Li, Dual-channel charges transfer strategy with synergistic effect of Z-scheme heterojunction and LSPR effect for enhanced quasi-full-spectrum photocatalytic bacterial inactivation: new insight into interfacial charge transfer and molecular oxygen activation, Appl. Catal. B 264 (2020) 118465.
[12] Q.L. Zeng, X.F. Xie, X. Wang, Y. Wang, G.H. Lu, D.Y.H. Pui, J. Sun, Enhanced photocatalytic performance of $Ag@TiO_2$ for the gaseous acetaldehyde photodegradation under fluorescent lamp, Chem. Eng. J. 341 (2018) 83–92.
[13] K. Wetchakun, N. Wetchakun, S. Sakulsermsuk, An overview of solar/visible light-driven heterogeneous photocatalysis for water purification: TiO_2- and ZnO-based photocatalysts used in suspension photoreactors, J. Ind. Eng. Chem. 71 (2019)

19–49.
[14] S. Kment, F. Riboni, S. Pausova, L. Wang, L.Y. Wang, H. Han, Z. Hubicka, J. Krysa, P. Schmuki, R. Zboril, Photoanodes based on TiO_2 and alpha-Fe_2O_3 for solar water splitting - superior role of 1D nanoarchitectures and of combined heterostructures, Chem. Soc. Rev. 46 (2017) 3716–3769.
[15] L.L. Peng, T.F. Xie, Y.C. Lu, H.M. Fan, D.J. Wang, Synthesis, photoelectric properties and photocatalytic activity of the Fe_2O_3/TiO_2 heterogeneous photocatalysts, Phys. Chem. Chem. Phys. 12 (2010) 8033–8041.
[16] M. Nasirian, M. Mehrvar, Photocatalytic degradation of aqueous methyl orange using a novel Ag/TiO_2/Fe_2O_3 photocatalyst prepared by UV-assisted thermal synthesis, Desalin. Water Treat. 137 (2019) 371–380.
[17] A. Laplaza, E. Jimenez-Relinque, J. Campos, M. Castellote, Photocatalytic behavior of colored mortars containing TiO_2 and iron oxide based pigments, Constr. Build. Mater. 144 (2017) 300–310.
[18] X. Dai, G. Lu, Y. Hu, X. Xie, X. Wang, J. Sun, Reversible redox behavior of Fe_2O_3/TiO_2 composites in the gaseous photodegradation process, Ceram. Int. 45 (2019) 13187–13192.
[19] Z.Y. Lin, P. Liu, J.H. Yan, G.W. Yang, Matching energy levels between TiO_2 and alpha- Fe_2O_3 in a core-shell nanoparticle for visible-light photocatalysis, J. Mater. Chem. A 3 (2015) 14853–14863.
[20] A. Banisharif, A.A. Khodadadi, Y. Mortazavi, A.A. Firooz, J. Beheshtian, S. Agah, S. Menbari, Highly active Fe_2O_3-doped TiO_2 photocatalyst for degradation of trichloroethylene in air under UV and visible light irradiation: experimental and computational studies, Appl. Catal. B-Environ. 165 (2015) 209–221.
[21] H. Zhao, W. Fu, H. Yang, Y. Xu, W. Zhao, Y. Zhang, H. Chen, Q. Jing, X. Qi, J. Cao, X. Zhou, Y. Li, Synthesis and characterization of TiO_2/Fe_2O_3 core–shell nanocomposition film and their photoelectrochemical property, Appl. Surf. Sci. 257 (2011) 8778–8783.
[22] S.J.A. Moniz, S.A. Shevlin, X. An, Z.-X. Guo, J. Tang, Fe_2O_3-TiO_2 nanocomposites for enhanced charge separation and photocatalytic activity, Chem. Eur. J. 20 (2014) 15571–15579.
[23] S.S. Kim, T. Van Khai, V. Kulish, Y.-H. Kim, H.G. Na, A. katoch, M. Osada, P. Wu, H.W. Kim, Tunable bandgap narrowing induced by controlled molecular thickness in 2D Mica nanosheets, Chem. Mater. 27 (2015) 4222–4228.
[24] Y.H. Zhang, Z.R. Tang, X.Z. Fu, Y.J. Xu, TiO2-graphene nanocomposites for gas-phase photocatalytic degradation of volatile aromatic pollutant: is TiO_2-Graphene truly different from other TiO_2-carbon composite materials? ACS Nano 4 (2010) 7303–7314.
[25] A.P. Grosvenor, B.A. Kobe, M.C. Biesinger, N.S. McIntyre, Investigation of multiplet splitting of Fe 2p XPS spectra and bonding in iron compounds, Surf. Interface Anal. 36 (2004) 1564–1574.
[26] Q. Mei, F. Zhang, N. Wang, Y. Yang, R. Wu, W. Wang, TiO_2/Fe_2O_3 heterostructures with enhanced photocatalytic reduction of Cr(vi) under visible light irradiation, RSC Adv. 9 (2019) 22764–22771.
[27] F. Mou, L. Xu, H. Ma, J. Guan, D.-R. Chen, S. Wang, Facile preparation of magnetic gamma- Fe_2O_3/TiO_2 Janus hollow bowls with efficient visible-light photocatalytic activities by asymmetric shrinkage, Nanoscale 4 (2012) 4650–4657.
[28] S.R. Mirmasoomi, M.M. Ghazi, M. Galedari, Photocatalytic degradation of diazinon under visible light using TiO_2/Fe_2O_3 nanocomposite synthesized by ultrasonic-assisted impregnation method, Sep. Purif. Technol. 175 (2017) 418–427.
[29] M. Yoon, M. Seo, C. Jeong, J.H. Jang, K.S. Jeon, Synthesis of liposome-templated titania nanodisks: optical properties and photocatalytic activities, Chem. Mater. 17 (2005) 6069–6079.
[30] S. Zuo, Z. Liu, W. Liu, X. Li, Z. Li, C. Yao, Q. Chen, Y. Fu, TiO_2 nanorod arrays on the conductive mica combine photoelectrochemical cathodic protection with barrier properties, J. Alloys. Compd. 776 (2019) 529–535.
[31] W.J. Lin, X.F. Xie, X. Wang, Y. Wang, D. Segets, J. Sun, Efficient adsorption and sustainable degradation of gaseous acetaldehyde and o-xylene using rGO-TiO_2 photocatalyst, Chem. Eng. J. 349 (2018) 708–718.
[32] Z. Zhang, Z. Jiang, W. Shangguan, Low-temperature catalysis for VOCs removal in technology and application: a state-of-the-art review, Catal. Today 264 (2016) 270–278.
[33] J.G. Yu, H.G. Yu, B. Cheng, X.J. Zhao, J.C. Yu, W.K. Ho, The effect of calcination temperature on the surface microstructure and photocatalytic activity of TiO_2 thin films prepared by liquid phase deposition, J. Phys. Chem. B 107 (2003) 13871–13879.
[34] Y. Yu, J.C. Yu, C.Y. Chan, Y.K. Che, J.C. Zhao, L. Ding, W.K. Ge, P.K. Wong, Enhancement of adsorption and photocatalytic activity of TiO_2 by using carbon nanotubes for the treatment of azo dye, Appl Catal B-Environ 61 (2005) 1–11.
[35] R. Yuan, S. Wang, D. Liu, B. Zhou, Photocatalytic oxidation of methyl orange in water using Fe-Zn co-doped TiO2 under different wavelengths, Desalin. Water Treat. 105 (2018) 310–321.
[36] Y. Nosaka, A.Y. Nosaka, Generation and detection of reactive oxygen species in photocatalysis, Chem. Rev. 117 (2017) 11302–11336.
[37] W.J. Li, D.Z. Li, Y.M. Lin, P.X. Wang, W. Chen, X.Z. Fu, Y. Shao, Evidence for the active species involved in the photodegradation process of methyl orange on TiO_2, J Phys Chem C 116 (2012) 3552–3560.
[38] H. Guo, C.-G. Niu, C.-Y. Feng, C. Liang, L. Zhang, X.-J. Wen, Y. Yang, H.-Y. Liu, L. Li, L.-S. Lin, Steering exciton dissociation and charge migration in green synthetic oxygen-substituted ultrathin porous graphitic carbon nitride for boosted photocatalytic reactive oxygen species generation, Chem. Eng. J. 385 (2020) 123919.
[39] X.K. Zeng, Z.Y. Wang, N. Meng, D.T. McCarthy, A. Deletic, J.H. Pan, X.W. Zhang, Highly dispersed TiO_2 nanocrystals and carbon dots on reduced graphene oxide: ternary nanocomposites for accelerated photocatalytic water disinfection, Appl. Catal. B-Environ. 202 (2017) 33–41.
[40] W. Liu, J.R. Ni, X.C. Yin, Synergy of photocatalysis and adsorption for simultaneous removal of Cr(VI) and Cr(III) with TiO_2 and titanate nanotubes, Water Res. 53 (2014) 12–25.